

INTENSE STAR-FORMATION AND FEEDBACK AT HIGH REDSHIFT: SPATIALLY-RESOLVED PROPERTIES OF THE $Z = 2.6$ SUBMILLIMETER GALAXY SMMJ14011+0252¹

N. P. H. NESVADBA^{2,3}, M. D. LEHNERT^{2,3}, R. GENZEL^{2,4}, F. EISENHAEUER², A. J. BAKER^{5,6}, S. SEITZ^{2,7}, R. DAVIES²,
D. LUTZ², L. TACCONI², M. TECZA⁸, R. BENDER^{2,7}, R. ABUTER⁹

Draft version December 2, 2024

ABSTRACT

We present a detailed analysis of the spatially-resolved properties of the lensed submillimeter galaxy SMMJ14011+0252 at $z=2.56$, combining deep near-infrared integral-field data obtained with SPIFFI on the VLT with other multi-wavelength data sets. As previously discussed by other authors, the broad characteristics of SMMJ14011+0252 in particular and submillimeter galaxies in general are in agreement with what is expected for the early evolution of local massive spheroidal galaxies. From continuum and line flux, velocity, and dispersion maps, we measure the kinematics, star-formation rates, gas densities, and extinction for individual subcomponents. The star formation intensity is similar to low-redshift “maximal starbursts”, while the line fluxes and the dynamics of the emission line gas provide direct evidence for a starburst-driven wind with physical properties very similar to local superwinds. We also find circumstantial evidence for “self-regulated” star formation within J1. The relative velocity of the bluer companion J2 yields a dynamical mass estimate for J1 within ~ 20 kpc, $M_{dyn} \sim 1 \times 10^{11} M_{\odot}$. The relative metallicity of J2 is 0.4 dex lower than in J1n/s, suggesting different star formation histories. SED fitting of the continuum peak J1c confirms and substantiates previous suggestions that this component is a $z=0.25$ interloper. When removing J1c, the stellar continuum and $H\alpha$ line emission appear well aligned spatially in two individual components J1n and J1s, and coincide with two kinematically distinct regions in the velocity map, which might well indicate a merging system. This highlights the close similarity between SMGs and ULIRGs, which are often merger-driven maximal starbursts, and suggests that the intrinsic mechanisms of star-formation and related feedback are in fact similar to low-redshift strongly star-forming systems.

Subject headings: galaxies: evolution — galaxies: kinematics and dynamics —

1. INTRODUCTION

Half of the stars in the local universe formed at $z \gtrsim 1$ or by about half the age of the universe (e.g., Rudnick et al. 2003, and references therein). However, in spite of our knowledge of “when”, our understanding of the physical processes triggering and governing this star formation is still rudimentary. In particular, does the physics of star formation depend on redshift? For example, Goldader et al. (2002) hypothesize that the intense star formation observed in some high-redshift galaxies might require a more efficient mode to form stars, without trig-

gering by major mergers. Erb et al. (2006), on the other hand, find that star formation in galaxies at $z \sim 2$ is less efficient, because they drive very efficient winds and energy into galaxy halos and the inter-galactic medium (IGM) and thus lose significant amounts of mass. Both hypotheses illustrate the need for detailed studies of star formation at high-redshift, to investigate whether low-redshift star-forming galaxies observed at high spectral and physical resolution can be good analogs to star formation at high redshift.

“Superwinds” – vigorous outflows of hot gas due to the thermalized ejecta of supernovae and massive stars in starburst galaxies – are inexorably linked to star formation. While winds likely play a fundamental role in galaxy formation and evolution (e.g., Heckman et al. 1990; Lehnert & Heckman 1996a), and contribute significantly to the metal content of the IGM (e.g., Bouché et al. 2005), the direct observational evidence for the ubiquity of winds in star-forming galaxies at high redshift is still rather limited. It is mainly based on blue line asymmetries and offsets of rest-frame UV interstellar absorption lines relative to optical emission lines (e.g., Pettini et al. 2001) and on the evolution of the mass-metallicity relationship at high redshift (Erb et al. 2006) in UV-selected galaxy populations.

Submillimeter galaxies (SMGs) at $z \sim 2$ are the sites of particularly vigorous star formation, with star-formation rates of $\sim 100 - 1000 M_{\odot} \text{ yr}^{-1}$, and thus provide an excellent opportunity to investigate the properties of extreme star formation at high redshift (Blain et al. 2002, and references therein).

¹ Based on observations collected at the European Southern Observatory, Very Large Telescope Array, Cerro Paranal, Chile (70.A-0254(A), 70.B-0545(A), and 073.A-5028(A)).

² Max-Planck-Institut für extraterrestrische Physik, Giessenbachstraße, D-85748 Garching bei München, Germany.

³ Current Address: Laboratoire Galaxies, Etoiles, Physique et Instrumentation, Observatoire de Paris, 5 place Jules Janssen, 92195 Meudon, France

⁴ Department of Physics, University of California, Berkeley, CA 94720.

⁵ Jansky Fellow, National Radio Astronomy Observatory, Department of Astronomy, University of Maryland, College Park, MD 20742-2421.

⁶ Current Address: Department of Physics and Astronomy Rutgers, the State University of New Jersey 136 Frelinghuysen Road Piscataway, NJ 08854-8019

⁷ Universitäts-Sternwarte, Scheinerstrasse 1, München D-81679, Germany.

⁸ University of Oxford, Subdepartment of Astrophysics, Denys Wilkinson Building, Keble Road, Oxfordshire, Oxford OX1 3RH, UK

⁹ European Southern Observatory, Karl Schwarzschild Straße, D-85748 Garching bei München, Germany

The $z=2.57^{10}$ SMG SMMJ14011+0252 (Iverson et al. 2001; Frayer et al. 1999) is perhaps the best studied SMG across all wavebands, because it has a relatively bright multiwavelength continuum, rest-frame optical emission lines with rather large equivalent widths, and moreover, is moderately gravitationally lensed ($\mathcal{M} \lesssim 5$) by the $z=0.25$ galaxy cluster A1835 (see Iverson et al. 2001; Barger et al. 1999; Fabian et al. 2000; Iverson et al. 2000; Smail et al. 2000, 2002; Downes & Solomon 2003; Tecza et al. 2004; Swinbank et al. 2004; Motohara et al. 2005; Smail et al. 2005). Iverson et al. (2000) gave the first detailed description of the source properties, and estimate a far-infrared luminosity of $\mathcal{L}_{FIR} \sim 6 \times 10^{12} L_{\odot}$ and a star-formation rate $SFR=1260-3900 M_{\odot} \text{ yr}^{-1}$ (for a magnification of 3; see also Iverson et al. 2001). Tecza et al. (2004) re-analyzed the FIR data given in Iverson et al. (2000), estimating $\mathcal{L}_{FIR} \sim 2.3 \times 10^{13} \mathcal{M}^{-1} L_{\odot}$ and FIR star-formation rates $\sim 1920 \mathcal{M}^{-1} M_{\odot} \text{ yr}^{-1}$, where \mathcal{M} indicates the magnification by the gravitational lens. The differences are mainly due to different assumptions regarding the modelling of the spectral energy distributions in the far-infrared and different initial mass functions for the star-formation rates. Since the values used in Tecza et al. (2004) are better matched to the assumptions made in our paper, we will in the following use the values of Tecza et al. (2004).

Many SMGs show evidence for optically evident AGN through their rest-frame optical line ratios (Takata et al. 2006). Swinbank et al. (2005) interpret the broad recombination line profiles in some SMGs as likely originating from nuclear broad line regions. Deep photometry of SMMJ14011+0252 covers X-ray to radio wavelengths, and longslit spectroscopy has previously been taken in the rest-frame UV and optical range. None of these data have revealed evidence for an AGN in this source. All these arguments make SMMJ14011+0252 an ideal target to study the properties of strongly star-forming galaxies in the early universe.

The relationship of the molecular gas relative to other components of SMMJ14011+0252 however has led to controversy in the literature. Frayer et al. (1999) reported the first detection of CO(3-2) emission, and Iverson et al. (2001) emphasize a good alignment of the CO(3-2) emission with the faint red component J1n, indicating that this is the location of the intense submm emission and the starburst (see Fig. 1 for the labeling). This view was later challenged by Downes & Solomon (2003), who found a different alignment of their CO(7-6) and CO(3-2) data sets with the rest-frame UV data, placing the CO emission significantly outside the optical emission of J1. The CO emission is marginally resolved spatially ($2'' \times < 0.4''$; Downes & Solomon 2003), and its line width of $FWHM = 190 \pm 10 \text{ km s}^{-1}$ corresponds to a dynamical mass of $3 \times 10^9 M_{\odot}$ (Greve et al. 2005, not correcting for inclination). We note that this mass estimate is less than the estimate of the total molecular mass of SMMJ14011+0252 (Frayer et al. 1999; Downes & Solomon 2003).

High-resolution HST F702W imaging shows that

¹⁰ Using the flat $\Omega_{\Lambda} = 0.7$ cosmology with $H_0 = 70 \text{ km s}^{-1} \text{ Mpc}^{-1}$ leads to $D_L = 21.04 \text{ Gpc}$ and $D_A = 1.66 \text{ Gpc}$ at $z = 2.565$. The size scale is $8.03 \text{ kpc}''$. The age of the universe for this redshift and cosmological model is 2.5 Gyrs.

SMMJ14011+0252 has a complex morphology in the rest-frame UV, which does not become more regular in rest-frame optical wavebands (Iverson et al. 2000). Based on rest-frame UV spectroscopy, Iverson et al. (2000) were the first to argue that the nearby blue component J2 is at a very similar but not identical redshift, and is a physically related component of J1. The nature of the bright UV-optical continuum peak J1c remained more mysterious: Downes & Solomon (2003) proposed that J1c might be a member galaxy of the foreground cluster A1835 along the line of sight and suggested that several blue features of J1 were in fact multiple images caused by strong lensing through a foreground source J1c. Smail et al. (2005); Swinbank et al. (2004) agree with the interpretation that J1c is a foreground source, but favor a lower magnification factors $\mathcal{M} \sim 3-5$, which would not lead to multiple images or strong differential lensing. They argue that absorption lines seen in the spectrum of Barger et al. (1999) can be identified as rest-frame optical absorption lines at $z \sim 0.25$, and highlight the nearly spherical morphology of J1c, both of which seem unlikely, if it is a lensed galaxy at $z=2.57$.

In a previous paper (Tecza et al. 2004, hereafter Paper I), we presented an initial analysis of deep near-infrared integral field spectroscopy of SMMJ14011+0252 obtained with SPIFFI on the VLT, concentrating on the integrated properties of the source, such as the high gas-phase oxygen abundance ($12 + [\text{O}/\text{H}] = 9.0$, measured with R_{23}) and large mass, and put these results into a broader perspective of mass assembly in the early universe within hierarchical structure formation models. We complement these findings now through a detailed analysis of the spatially-resolved properties of this source, and we particularly discuss the implications for star formation and related feedback in massive galaxies at high redshift.

2. SPIFFI AND COMPLEMENTARY DATA SETS

SMMJ14011+0252 was observed in the J, H and K-bands with the integral field spectrometer SPIFFI (Eisenhauer et al. 2003) at the ESO VLT in spring 2003, with individual exposure times of 300 s in H, and 600 s in J and K. Total exposure times were 340 min in K, 95 min in H and 60 min in J. We used the $0.25''$ pixel scale and obtained spectral resolutions of $R = \frac{\lambda}{\Delta\lambda} \sim 1500$ in the J-, ~ 2000 in the H-, and ~ 2400 in K-bands.

The data were calibrated using the UKIRT faint standard FS135 and agree to within a few percent with the magnitudes previously published for SMMJ14011+0252 (Iverson et al. 2000). The seeing disk has $FWHM = 0.6'' \times 0.4''$ in right ascension and declination, respectively and was measured from the standard star. The data reduction has been described elsewhere (Nesvadba et al. 2006a). The main difference between the data reduction in this paper and Paper I is improved sky subtraction allowing us to investigate the spatially-resolved properties of SMMJ14011+0252 more robustly. The previous reduction algorithm led to an effective oversubtraction of the sky background near bright emission lines. As a result, the data quality in individual frames was improved through the new reduction, which yielded a more accurate alignment of the individual frames, which led to a better data quality in the combined data set and a better spatial resolution. This has no significant impact on the

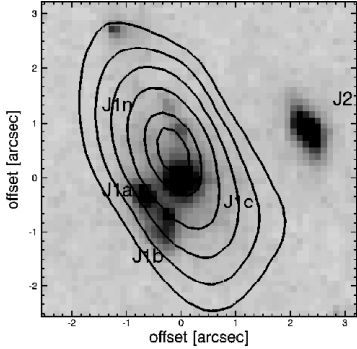


FIG. 1.— Contours showing the distribution of the CO(3-2) line emission superimposed on the F702W WFPC2 broad band continuum image (shown in grayscale). The CO(3-2) map is from Downes (2006) and the labels on the WFPC2 image designate the regions of SMM14011+0252 following the scheme of Motohara et al. (2005). J1n refers to the diffuse extended region north of J1c (see also Fig. 2). North is up and east is to the left. The astrometry used for this overlay was derived from identifying 6 radio sources in the FORS V-band image (see text for details).

integrated spectrum discussed in Tecza et al. (2004), but does change the mapping of kinematics and emission line morphologies by improving the signal-to-noise of the low surface brightness line emitting regions.

In addition, before and since the publication of Paper I, a large number of complementary data sets are (now) available to supplement and refine the interpretation of the SPIFFI data and the overall nature of the source. Ivison et al. (2001) obtained high-resolution optical imaging of the A1835 field through the F702W ($\equiv R_{702}$) filter of the WFPC2 on-board the HST. The reduced image was kindly provided by R. Ivison. He also kindly shared his 1.4 GHz continuum map of A1835 with us, which was obtained with the NRAO Very Large Array (VLA; Ivison et al. 2001). D. Downes kindly provided us with his CO (3–2) and 242 GHz continuum maps of SMMJ14011+0252 obtained with the IRAM Plateau de Bure Interferometer (PdBI; Downes & Solomon 2003).

Deep ISAAC J, H, and K band images are available from the ESO archive and were reduced as described in Bremer et al. (2004). A deep VLT FORS1 V-band image of the field of A1835 was obtained, reduced, and is described in Lehnert et al. (2005). A. Barger kindly provided the rest-frame UV spectra taken with LRIS on the Keck 10m telescope and published in Barger et al. (1999). Finally, R. Pello and A. Hempel graciously shared their F850LP ($\equiv Z_{850}$) ACS image of SMMJ14011+0252 J1 and J2 before the data were publicly available.

3. ABSOLUTE ASTROMETRY

Various possible and disparate alignments have been proposed for SMMJ14011+0252 in the literature (cf. Downes & Solomon 2003; Ivison et al. 2001). The position of both the radio and mm interferometric positions relative to the rest-frame optical and UV have been especially problematic.

We obtained a new and more robust astrometry for the field of SMMJ14011+0252 using ISAAC K-band and FORS V-band imaging of A1835 (Lehnert et al. 2005). We identified six radio sources in the V-band image at magnitudes brighter than 17.5 mag (the V-band image

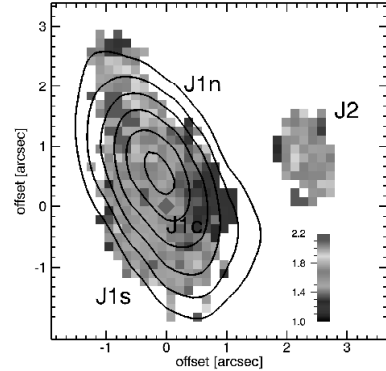


FIG. 2.— The J–K color distribution with superimposed contours showing the CO(3-2) flux distribution map. North is up and east is to the left. From our own lensing models and those of Smail et al. (2005), the direction of the largest lensing shear is roughly along the axes of largest extent in J1 and J2. J band emission in J1n is below the 3σ limit in $\sim 10\%$ of the pixels where K band emission is detected. The reddest area in J1n therefore represents a 3σ lower limit on the intrinsic J–K color.

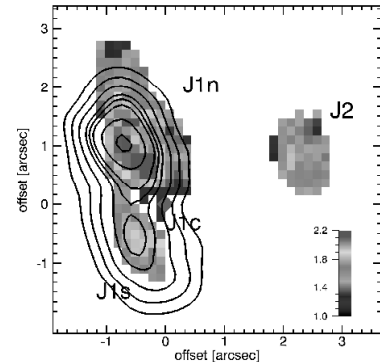


FIG. 3.— J–K color distribution of SMMJ14011+0252 as in Fig. 2 but with the model of J1c removed. Contours indicate H α line emission in steps of 2σ with the lowest contour representing 3σ . The contribution of strong H α emission has been removed when calculating the J–K colors. North is up, east to the left.

has a 5σ limit of 27.8 mag). Of these 6 sources, 3 were point sources at the resolution of the data (seeing FWHM ~ 0.7 – 0.8 arcsec) and 3 were extended. Given their high signal-to-noise, the uncertainty in the position is very small ($\lesssim 0.08$ arcsec). The depth and field of view of this image are greater than previously available optical/near-infrared data. The radio sources are spread over the roughly $6' \times 6'$ field of view of the V-band image. A comparison of the radio source and optical positions suggests that the best alignment has an RMS scatter of $0.04'' \times 0.08''$ ($\sim 10\times$ less than the absolute positional uncertainty in each band). Such a good alignment suggests that both the position in each frame can be accurately determined and that the relative distortion in both the radio map and V-band image are insignificant compared to the total relative positional uncertainties over the entire field of view of the V-band image. All other optical/NIR data can be referenced to the V-band image to a very high accuracy given the large number of sources that we used for the relative alignment (several dozen point or point-like sources). The VLA radio and PdBI millimeter maps share the “radio” coordinate frame. We estimate a total absolute uncertainty of $0.33'' \times 0.34''$ ($\lesssim 1.5$ SPIFFI pixels) in right ascension and declination

of the optical and near-infrared data relative to the CO position, including an absolute astrometric uncertainty in the CO map of $0.3''$ (following Downes & Solomon 2003) and a fiducial uncertainty of $0.14''$ (the pixel size of the ISAAC data, which is certainly an over-estimate of the true uncertainty since the relative alignment is better than a pixel). The relative uncertainty between the VLA map and the optical/near-infrared data is smaller (by a factor of 4 to 8).

The aligned K-band ISAAC image was used to put the SPIFFI cubes into the common frame, based on the positions of J1 and J2 and assuming a pixel scale of $0.25''$ for the SPIFFI data. J1 and J2 have signal-to-noise ratios >15 and 6 in the SPIFFI continuum image in the central pixel, respectively, and signal-to-noise ratios >30 and 11 in the ISAAC K band image, respectively. The alignment is limited by the uncertainty of the peak position in J1c and J2, which is much smaller than a single pixel in either data set ($0.25''$ for SPIFFI or $0.14''$ for ISAAC).

Our new astrometric alignment rules out previous claims that the CO emission might be significantly offset from the UV and optical positions, and is an independent confirmation of the initial alignment of Ivison et al. (2001), based on some new data sets. The position of the CO data is shown in Fig. 1 as contours overlaid on the HST R_{702} image, and in Fig. 2 with respect to the ISAAC J–K color image. Within the uncertainty of $0.33''$ the CO emitter can be identified with either J1n or J1c. The redder colors and stronger star formation (§5.1) favor J1n as the more likely source of CO line emission. We summarize the positions of the individual components in SMMJ14011+0252 relative to the radio frame in Table 1. At any rate, this calibration firmly places the CO and radio emission within the isophotes of J1 in the HST (Ivison et al. 2000) and ground-based images (Ivison et al. 2000; Bremer et al. 2004; Lehnert et al. 2005).

4. RESULTS AND ANALYSIS

4.1. Continuum Morphology and Colors

The rest-frame optical and UV continuum and H α emission line morphology of the J1 complex have been described elsewhere (see, e.g. Ivison et al. 2000; Tecza et al. 2004; Motohara et al. 2005; Smail et al. 2005). Overall, our data are consistent with these previous descriptions, but deeper and more detailed in several aspects. We label individual components in Fig. 1–3.

Continuum emission is centered on J1c and varies strongly with wavelength. At short wavelengths J1c is small and highly symmetric. At longer wavelengths the extended emission becomes relatively stronger. In Fig. 2 we show the J–K band color distribution derived from the ISAAC data. The K band data were convolved with a two-dimensional Gaussian disk to have the same resolution as the J band data. K band fluxes are corrected for the H α equivalent width measured with SPIFFI. Line contamination is <0.2 mag in J1n and insignificant in J1s.

J–K colors (corresponding to roughly $U - R$ at rest-frame) are different in J1n and J1s, with $J-K \approx 1.6$ in J1s. J band emission in J1n is relatively faint. We replaced the J band flux by the 3σ limit where we detected K, but no J band emission, so that the measured $J-K \approx 2.0$ in J1n is in fact a lower bound to the $J-K$

TABLE 1
SMMJ14011+0252: ASTROMETRY

Component	R.A.(2000) (2)	Decl.(2000) (3)	Δ_{RA}^{J1c} (4)	Δ_{Dec}^{J1c} (5)	Data (6)
J1c	14:01:04.933	02:52:23.98	0.0	0.0	F702W
J1a	14:01:04.967	02:52:23.73	0.51	0.25	F702W
J1b	14:01:04.948	02:52:23.43	0.22	0.55	F702W
J1n	14:01:04.969	02:52:24.81	0.54	0.83	SPIFFI
1.4GHz	14:01:04.92	02:52:24.80	0.20	0.83	I01
PdBI 1mm	14:01:04.933	02:52:24.20	0.00	0.22	D06
PdBI 3mm	14:01:04.933	02:52:24.37	0.00	0.39	D06
J2	14:01:04.806	02:52:24.73	1.90	0.75	F702W

NOTE. — Absolute positions in the radio frame of subcomponents from our revised astrometry. Uncertainties in the relative alignment of the CO are $\sim 0.33''$. Column (1) – Designations of the various regions defined with SMMJ14011+0252. In the text, since a majority of the data sets do not resolve J1a and J1b, we have used the designation J1s for the combined and surrounding emission of J1a and J1b. Column (2) – Right ascension. Column (3) – Declination. Column (4) – Relative offset to J1c in right ascension in arcsec. Column (5) – Relative offset to J1c in declination in arcsec. Column (6) – Data set used for measurement. F702W – WFPC2 data of Ivison et al. (2000). I01 – VLA 1.4 GHz radio data of Ivison et al. (2001) – D06 – PdBI CO data of Downes (2006, and private communication of currently unpublished data sets). SPIFFI – K-band IFU data set.

color in J1n.

The red area in J1s coincides spatially with the bright knots J1a and J1b in the HST F702W image. We also identify these knots in the ISAAC K-band image. Comparison of the seeing-matched ISAAC and HST data sets indicates that the prominence of these knots in the HST data compared to the ground based images is in large parts due to the smaller PSF in the F702W image and does not reflect intrinsic variations in size with wavelength or strong line contamination. Unresolved blue knots superimposed on J1n in Fig. 3, however, should also appear at longer wavelength in spite of the lower resolution. We do not observe them while the low surface brightness region becomes more prominent in J1n. This indicates that these color variations reflect intrinsic variations in the morphology of J1n.

4.1.1. Line Ratio Diagnostics: Ionizing Source and Gas Densities

Line emission in J1 reaches the highest surface brightnesses in the areas of J1n and J1s, and is generally lower in J1c, as expected for a foreground galaxy. To differentiate between J1n and J1s, we assign all spatial pixels to J1n and J1s, if they are at least two SPIFFI pixels ($0.5''$, roughly corresponding to the seeing disk) north or south from J1c, respectively. The spectral range of our observations includes all strong optical emission lines between the [OII] $\lambda 3726, 3729$ and the [SII] $\lambda 6717, 6731$ doublets. We use emission line ratios, namely [OIII]/H β , [NII]/H α , and [SII]/H α to constrain the ionizing source (e.g. Baldwin et al. 1981). All line ratios in the two-dimensional diagnostic diagrams are within the region of HII regions for all components. J1n falls on the dividing line between HII regions and LINERS (Osterbrock 1989), similar to many other high-redshift sources showing high excitation (Erb et al. 2006; van Dokkum et al. 2005). This indicates that the bulk of the line emission in J1n and J1s arises from gas photoionized by hot massive stars and supports earlier X-ray measurements

(Fabian et al. 2000), that the far-infrared emission from this system is powered by the starburst, without a measurable AGN component.

The $H\alpha$ emission lines in J1n and J1s have a relative spectral shift of $61 \pm 9 \text{ km s}^{-1}$, significant at the level of $\sim 6\sigma$. $[\text{NII}]/H\alpha$ ratios are 0.52 ± 0.03 and 0.43 ± 0.02 in the integrated spectra of J1n and J1s, respectively. Line widths (and 1σ scatter of individual line width measurements) are $\text{FWHM} = 198 \pm 32 \text{ km s}^{-1}$ in J1n, and are marginally narrower in J1s ($\text{FWHM} = 157 \pm 35 \text{ km s}^{-1}$) with large scatter across both components. We summarize the emission line properties in Table 2.

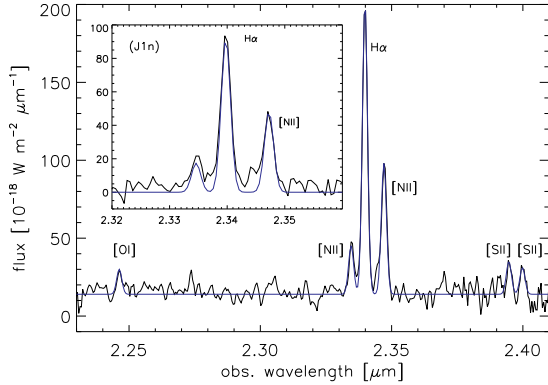


FIG. 4.— Integrated K band spectrum of J1n, showing the detected emission lines: $[\text{OI}]\lambda 6300$, $[\text{NII}]\lambda 6548$, $H\alpha$, $[\text{NII}]\lambda 6583$, and the $[\text{SII}]\lambda\lambda 6717, 6730$ doublet. Gaussian line fits are shown in blue, for all lines we assumed the FWHM and redshift measured for $H\alpha$. The inset shows a zoom onto the $H\alpha$ and $[\text{NII}]\lambda 6583$.

We calculate the extinction in the two regions from the observed $H\alpha/H\beta$ ratios (see Table 2), the Balmer decrement, and a Galactic extinction law, as described in Paper I, and extract the $H\beta$ line emission from the same regions as $H\alpha$. For J1n and J1s, we find $E(B - V) = 1.6$ and 1.3, respectively.

The $[\text{OII}]\lambda 3726, 3729$ and $[\text{SII}]\lambda 6717, 6731$ doublets are faint, but are spectrally resolved and have sufficient signal-to-noise ratios in the integrated spectrum to robustly measure the ratios of the two components, $R_{[\text{SII}]} = I(6717)/I(6731) = 1.25 \pm 0.18$ and $R_{[\text{OII}]} = I(3726)/I(3729) = 1.07 \pm 0.21$ for $[\text{SII}]$ and $[\text{OII}]$, respectively (see Table 2). For densities between 100 and 10^5 cm^{-3} and a given temperature, the ratio of the two components yields the electron densities. Assuming a “canonical” temperature $T = 10^4 \text{ K}$ for HII regions (Osterbrock 1989), our best-fit density estimate $N_e \sim 400 \text{ cm}^{-3}$ (with favored values between ~ 180 and 900 cm^{-3} , see Fig. 5)

4.2. Morphology and Kinematics of the Emission Line Gas: Evidence for a Merger?

Fig. 1 of Paper I shows the continuum-subtracted $H\alpha$ line image extracted from the SPIFFI data cube. $H\alpha$ emission is extended both along and perpendicular to the direction of lensing shear in the two components of SMM14011+0252, J1 and J2. $H\alpha$ line emission is detected in J1n and J1s.

The SPIFFI K-band integral-field spectroscopy of J1 is of superb quality and allows us to map the intrinsic kine-

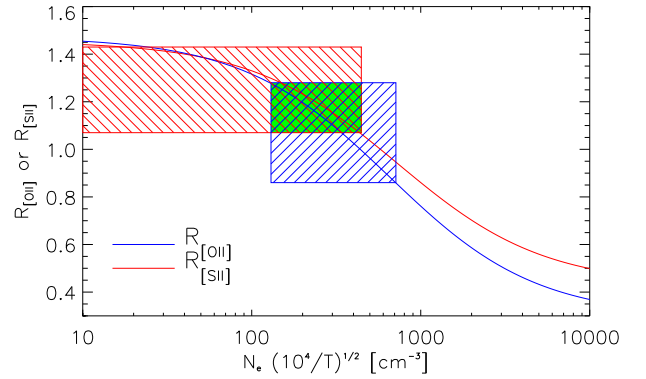


FIG. 5.— Density estimates in SMM14011+0252 J1n as a function of line ratio for the $[\text{OII}]\lambda\lambda 3726, 3729$, $R_{[\text{OII}]}$ (blue line), and $[\text{SII}]\lambda\lambda 6716, 6731$, $R_{[\text{SII}]}$ (red line), doublets, scaled to a temperature $T_e = 10^4 \text{ K}$. The red and blue shaded regions show the ranges of line ratios and densities for the $[\text{OII}]$ and $[\text{SII}]$ doublets respectively. The green shaded region shows the overlap of best fit density considering both doublets. The sizes of the boxes along the ordinate represent the range of 1σ uncertainties in each line ratio while the sizes of the boxes along the abscissa represent the range of densities permitted by their respective curves of density versus R .

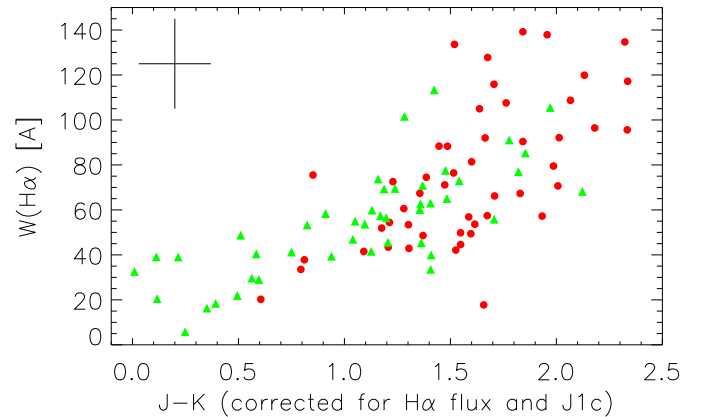


FIG. 6.— Rest-frame equivalent widths (in \AA , positive values indicate line emission) plotted versus the J-K color. The contribution of strong $H\alpha$ emission has been removed when calculating the J-K color, and we used the J1c removed colors. Pixels that comprise J1s, and J1n, are shown as solid green triangles, and solid red circles, respectively. The cross indicates the typical uncertainties.

matics within J1 using the spectral positions of the $H\alpha$ line cores (fitted with Gaussian line profiles) across an area of $1.75'' \times 3.25''$, with uncertainties of $\lesssim 15 \text{ km s}^{-1}$ (Fig. 7). With a spatial resolution of $0.4'' \times 0.6''$ in right ascension and declination, respectively, corresponding to $\sim 4.4 \times 5.4$ seeing disks. Hence, the data set is well resolved spatially. Velocity dispersions of the lines are $\sigma = 55 - 106 \text{ km s}^{-1}$ (corrected for the instrumental resolution). Velocities vary by 190 km s^{-1} with the steepest overall velocity gradient increasing from north-east to south-west. Although this gradient is continuous, it is not strictly monotonic, and the data suggest velocity shears along two axes, which coincide with the regions of maximum K band surface brightness in the J1c removed data sets (Fig. 7). The differences in the peak veloci-

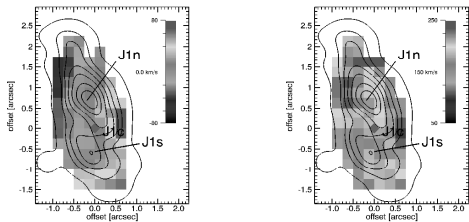


FIG. 7.— Map of relative velocities (*top*) of $H\alpha$ and full width at half maximum of $H\alpha$ (*bottom*). In both plots, contours indicate the K-band surface brightness with J1c removed, and the diamond indicates the location of J1c. North is up, east to the left in each panel.

ties in these two dynamical regions are highly significant ($> 3\sigma$) and are thus not consistent with a single velocity gradient.

The close spatial alignment between star-formation (traced by the $H\alpha$ surface brightness), gravitational potential (traced by the velocity map), and stellar population (traced by the K band continuum and $J-K$ color) is intriguing (Fig. 7). This coincidence of the velocity shear, star-formation, and K-band continuum can be naturally explained if J1n and J1s are a close, likely merging, galaxy pair. Moreover, this hypothesis is supported by our population synthesis fits discussed in §4.4, which imply that J1n and J1s are dominated by stellar populations of different ages and extinctions, and they have different velocity dispersions (Fig. 7). At a projected distance of $\sim 12M^{-1}$ kpc, the internal dynamics of J1n and J1s appear to be driven by their own gravity. The evidence for this is our finding that both have velocity gradients which align well with their axes of the most extended K-band continuum emission. This indicates that the central parts of either components are likely still dominated by their individual potential wells.

We have also mapped the $[\text{NII}]/H\alpha$ line ratios (Fig. 8) over most of J1, where both lines are detected at $> 5\sigma$ significance. Ratios are $[\text{NII}]/H\alpha \sim 0.3 - 0.4$ over most of J1s, in the typical range of metal-rich H II regions and galaxy nuclei in the nearby universe. $[\text{NII}]/H\alpha$ ratios peak in J1n, about $0.8''$ to the north from J1c, and $\sim 0.6''$ from the $H\alpha$ peak. The maximum ratio is $[\text{NII}]/H\alpha \sim 0.7$, which is significantly larger than the ratios generally found in HII regions (Pettini & Pagel 2004; Osterbrock 1989, and references therein), and is more typical of starburst nuclei in the local universe (e.g., Lehnert & Heckman 1996a). By analogy, this possibly indicates a strong shock component due to an outflow (see §6 for a detailed discussion). $[\text{OIII}]\lambda 5007$ and $H\beta$ are found (at lower signal-to-noise) near the $[\text{NII}]$ surface brightness peaks in J1n and J1s, consistent with this hypothesis.

4.3. Relationship between Gas and Continuum Emission

In both J1n and in J1s, the brightest $H\alpha$ emitting regions are also the regions with the reddest $J-K$ colors. Rest-frame equivalent widths are $\sim 50 - 150 \text{ \AA}$ and are positively correlated with $J-K$ color in J1n and J1s, with significances better than $\mathcal{O}(0.01)$ in non-parametric tests (low values indicate a highly significant correlation; Fig. 3). The positive correlation is a clear indication that the reddening is related to star-formation in regions with variable and high extinction rather than the age of the stellar population. If the red colors indicated the age of

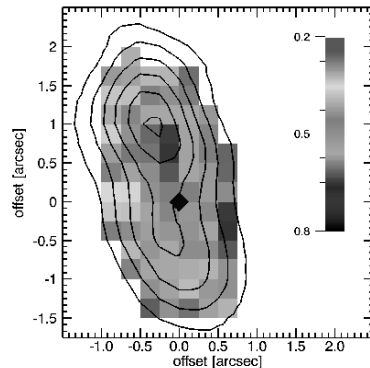


FIG. 8.— Map of the $[\text{NII}]\lambda 6583/H\alpha$ line ratios for the J1 complex. Contours indicate the distribution of $H\alpha$ line surface brightness. The grayscale bar on the right indicates the values of the $[\text{NII}]\lambda 6583/H\alpha$ ratios. North is up, east to the left. The diamond marks the position of J1c.

the stellar population, we would expect that the reddest regions of the galaxy in $J-K$ would be the ones with the lowest $H\alpha$ equivalent widths.

In the case of SMMJ14011+0252, however, the highest equivalent widths are reached in the reddest areas, indicating that the color is indeed due to variable and high extinction, rather than an age spread in the stellar populations in both J1n and J1s. In addition, where the surface brightness of line emission is intense enough to allow for a robust measure of $H\beta$, the reddest regions also have high $H\alpha/H\beta$ ratios. This supports the hypothesis that the color variation is more likely due to reddening than to large differences in ages of the stellar populations. Our finding also implies, however, that significant numbers of $H\alpha$ photons escape, perhaps a sign for an irregular, clumpy dust distribution. Chapman et al. (2004) reach a similar conclusion based on the differences in structure in high resolution radio maps compared to high resolution imaging in the rest-frame UV. It is also possible that a favorably oriented starburst-driven wind (§6) is giving a less obscured view to some of the starburst region.

4.4. Population Synthesis Models and the Role of J1c

As outlined in the Introduction, the nature of the optical and near-infrared continuum peak J1c is difficult to constrain. It has a nearly circular symmetry which led Smail et al. (2005) conclude that J1c cannot be gravitationally lensed and is thus not at the redshift of SMM14011+0252 (and in agreement with Swinbank et al. 2004, that some of absorption lines in the Barger et al. spectrum are coincident with optical absorption lines from a galaxy at $z=0.25$). Moreover, its smooth, featureless light profile does not appear typical for a strongly star-forming dusty galaxy at high redshift seen in the rest-frame UV. Both arguments, although circumstantial, imply that J1c could be a foreground object along the line of sight which is not physically related to the SMG. Unfortunately, the observed wavelengths of some of the optical absorption lines at the redshift of the foreground cluster A1835 are degenerate with UV absorption lines at the redshift of the SMG (Swinbank et al. 2004; Smail et al. 2005), so that the spectrum is not necessarily a unique constraint.

We constructed an azimuthally averaged light profile of J1c from the F850LP ACS image of SMMJ14011+0252.

To this one-dimensional profile, we fit a Sersic profile convolved with the PSF (estimated using a nearby star in the ACS image), obtaining a good fit with a Sersic model model of index $n = 1.25 \pm 0.2$ and a half-light radius, $r_e = 0.27'' \pm 0.06''$. The spatial resolution is $\sim 0.11''$. We then subtract this fit from the ACS image. Fit residuals are $\lesssim 10\%$ in a $0.5''$ box aperture centered on J1c, and are likely due to deviations in the core of the PSF from our simple Gaussian model and/or extended emission from the sources J1s and J1n contaminating the fitted light distribution of J1c. The left panel of Fig. 9 shows the J1c removed F850LP ACS image.

We estimate the impact of J1c in each waveband by convolving our best-fit Sersic model from the ACS image with the PSF appropriate for each individual band and scaling to the measured peak brightness of J1c. This scaled, smoothed Sersic model is then subtracted from each image centered on the position of J1c. Namely, we obtain magnitudes of $R_{702} = 20.6$ mag, $Z_{850} = 20.5$ mag, $J = 20.0$ mag, $H = 19.0$ mag, and $K = 18.2$ mag extracted from a $3''$ aperture centered on J1c in the HST F702W WFPC2 and F850LP ACS images, and the ISAAC J, H, and K band images, respectively. For the best-fit Sersic models to J1c, integrated over $3''$ apertures, we find $R_{702} = 21.5$ mag, $Z_{850} = 21.3$ mag, $J = 20.7$ mag, $H = 19.9$ mag, and $K = 19.2$ mag in these bands. We use the fit residuals in each band to constrain whether the light profile varies significantly with wavelength. Overall fit residuals are $\leq 15\text{-}20\%$ with random spatial distribution, consistent with a light profile of J1c that is not a strong function of wavelength (for illustration we use the K band data in the right panel of Fig. 9). Our goal is to give an upper limit on the overall impact of J1c on the submm source, which might lead to an oversubtraction and is conservative. However, doing the subtraction this way will lead to a region centered on J1c that is essentially at the background average in each image and appear as a hole in the source (Fig. 9). Thus the detailed morphology of J1n and J1s over the region of J1c should not be overinterpreted (i.e., the hole in the light distribution is likely not real and is not therefore a sign of strong shear for example). The S/N and rather coarse sampling in the SPIFFI data do not allow a similar correction for the spectra (except in the case of the $H\alpha$ equivalent widths that are enumerated in Fig. 6).

Deriving the magnitudes in the F702W, F850LP, J, H, and K bands based on the scaled Sersic model, we fit the SED of J1c using the stellar population synthesis package of Bruzual & Charlot (2003) for solar metallicity and a Chabrier IMF. The SED is consistent with that of a $z=0.25$ galaxy with an $\gtrsim 9$ Gyr old stellar population of total mass $\lesssim 5 \times 10^9 M_\odot$. We do not find any suitable model when placing J1c at $z \sim 2.6$, which supports the interloper hypothesis for J1c. For an isothermal sphere and assuming that the projected half light radius is the half mass radius of the galaxy, the stellar mass estimate corresponds to a velocity dispersion which is consistent with $\sigma \lesssim 55 \text{ km s}^{-1}$ adopted by Smail et al. (2005).

From the data sets with J1c removed, we investigate the stellar populations in J1s and J1n, assuming continuous star-formation histories, solar metallicity, and a Chabrier IMF. Using only one star-formation history and model is all that is justifiable given the considerable uncertainties in removing J1c, and the overall faintness

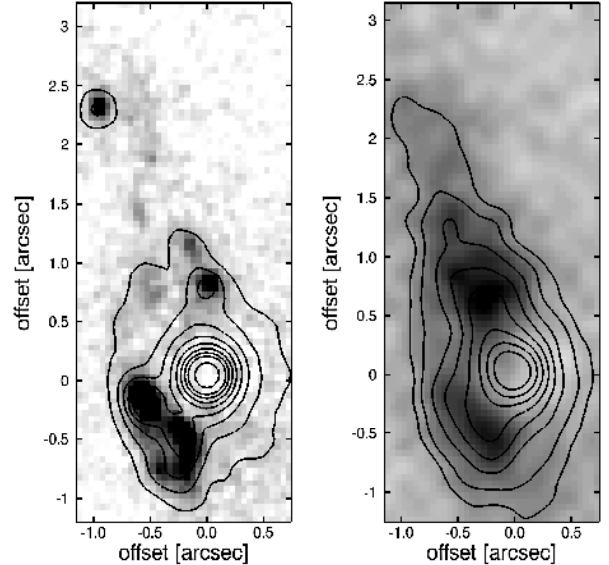


FIG. 9.— The light profile of J1c is very well fit with a Sersic profile. The left panel shows the fit residuals in the F850 ACS image, the right panel shows the residuals when subtracting the same, but seeing-matched, model from the K band image of J1, adopting the same pixel scale as in the ACS image. Contours indicate the original surface brightness distribution of the F850LP and K band images, respectively. The morphology of J1n and J1s over the region of the highest surface brightness region where J1c was located is an artifact of scaling the model to the peak of the surface brightness of J1c in each image.

of J1n and J1s. For J1s, our fits are consistent with a $\gtrsim 3 \times 10^8$ Gyr old stellar population in J1s, $A_V \sim 0.8$ mag extinction, and a mass of $\sim 8 \times 10^9 M_\odot$ (with the magnification factor \mathcal{M}). For J1n, we find a $\lesssim 1 \times 10^8$ yrs old stellar population, $A_V \gtrsim 6$ mags, and a stellar mass of about $3 \times 10^{10} M_\odot$. These age estimates are in approximate agreement with what would be estimated from the values of the rest-frame $H\alpha$ equivalent widths. Fig. 6 shows that the rest-frame equivalent widths of $H\alpha$ are typically about 80 and 120 Å for the most intense $H\alpha$ emitting regions of J1s and J1n respectively. Models of continuous star formation and solar metallicity imply ages of a few 100 Myrs or less, with higher equivalent widths corresponding to younger ages (Leitherer et al. 1999). The $H\alpha$ to $H\beta$ line ratios imply significant extinction in both J1n and J1s, as discussed in §4.1.1 and shown in Table 2.

These mass estimates are likely only lower limits. To isolate the individual components, we extract the photometry from square apertures with $1.5''$ on each side (which is at least twice the seeing disk in any of the images). From a sample of 20 SMGs and optically faint radio galaxies with ACS imaging, Smail et al. (2004) find half-light diameters $D_{1/2} \sim 1.5''\text{-}3''$. For $\mathcal{M}=3\text{-}5$ this implies that we are underestimating the stellar mass by a factor $\sim 2\text{-}6$, depending on the exact morphology and light profile of J1n. Moreover, our population synthesis fits might be biased by the strong and clumpy extinction discussed in §4.2. Consequently, we likely underestimate the overall age and extinction and hence the stellar mass. This also raises worries that a significant fraction of the total stellar population might be undetected due to strong extinction, if the most strongly dust-enshrouded

areas are optically thick to the rest-frame R-band continuum (observed K band). This concern of course generically applies to photometric studies of dusty high-redshift galaxies. Therefore analyzing spectra appears to be more promising for estimating the physical properties of these dusty systems.

We will in the following adopt $\gtrsim 6 \times 10^{10} \mathcal{M}^{-1} M_{\odot}$ as the stellar mass of J1n (correcting by a conservative factor ~ 2 due to light not considered in the SED fit). We warn that given the relatively crude manner in which this estimate was made, and the intrinsic difficulty in estimating the mass and star-formation properties in heavily obscured galaxies from UV/blue optical SEDs, our estimates are comparably uncertain.

5. CHARACTERISTICS OF A HIGH-REDSHIFT STARBURST

5.1. *Star-formation Intensity*

Observations of low-redshift starburst galaxies suggest a fundamental upper threshold for the star-formation rate in galaxies (Lehnert & Heckman 1996b; Meurer et al. 1997). Such an upper limit may be indicative of self-regulation processes limiting the gas collapse (and subsequent star-formation) through the negative feedback of superwinds (e.g., Lehnert & Heckman 1996b, see also §6) or perhaps dynamical processes and disk instabilities (e.g., Meurer et al. 1997). It is therefore interesting to investigate how SMMJ14011+0252 J1 relates to the “maximal burst” galaxies observed at low redshift.

For low-redshift star-forming galaxies, Meurer et al. (1997) propose an upper bound of $SFR_{max} \sim 45 M_{\odot} \text{ yr}^{-1} \text{ kpc}^{-2}$ within one half-light radius $r_{1/2}$. The exact value of the maximal star-formation intensity depends on the choice of cosmology, the form of the chosen initial mass function, the relative role of extinction, the ability to measure half-light radii accurately at wavelengths where a substantial fraction of the bolometric luminosity originates, etc., and thus the numerical value of this threshold should not be interpreted too strictly. However, it does provide a useful guide on when star-formation becomes “maximal” – whatever the cause (see also Lehnert & Heckman 1996a,b; Tacconi et al. 2006). Do extreme starbursts in high-redshift galaxies have similar intensities? We will in the following address this question empirically, comparing the star-formation intensity in SMMJ14011+0252 with low redshift starbursts (Lehnert & Heckman 1996b), using the same techniques. Such an estimate does not depend on the strength of the gravitational lensing, because surface brightness is conserved and $\lesssim 10\%$ of the $H\alpha$ emission is due to the wind component (§6), which is negligible.

We estimate the half-light area in $H\alpha$, $A_{1/2, J1n}^{H\alpha}$, by counting the pixels in J1n and J1s, respectively, that are above the 50% percentile of the flux distribution (following the method of Erb et al. 2003). In J1n and J1s we find $A_{1/2}^{J1n} = 1.1 \square''$ (68 kpc^2), and $A_{1/2}^{J1s} = 0.875 \square''$ (56 kpc^2), respectively. Using the measured $H\alpha/H\beta$ decrements from these regions to correct the $H\alpha$ emission line fluxes for extinction, we estimate intrinsic $H\alpha$ fluxes, $F_{J1n} = 1.1 \times 10^{-18} \text{ W m}^{-2}$ in J1n and $F_{J1s} = 0.37 \times 10^{-18} \text{ W m}^{-2}$ in J1s, respectively. We follow Kennicutt (1998) with a 1-100 M_{\odot} Salpeter IMF

to estimate star-formation rates, i.e. we adopt $SFR = 7.69 \times 10^{-35} \mathcal{L}_{H\alpha} M_{\odot} \text{ yr}^{-1}$, where the $H\alpha$ luminosity $\mathcal{L}_{H\alpha}$ is given in Watts. Our adopted IMF gives a total star-formation rate similar to that if we had adopted a more appropriate IMF such as a Kroupa or Chabrier, namely $450 \mathcal{M}^{-1} M_{\odot} \text{ yr}^{-1}$ in J1n and $150 \mathcal{M}^{-1} M_{\odot} \text{ yr}^{-1}$ in J1s, respectively. We thus find star-formation rate densities of $7 M_{\odot} \text{ yr}^{-1} \text{ kpc}^{-2}$ in J1n and $3 M_{\odot} \text{ yr}^{-1} \text{ kpc}^{-2}$ in J1s, respectively. In either case, the intensities are well below the limit suggested by Meurer et al. (1997).

Star-formation rates based on $H\alpha$ luminosities tend to be lower by up to about an order of magnitude compared to estimates based on infrared luminosities. This is because the most intense star-forming regions are likely to be optically thick to dust at the wavelength of $H\alpha$, so that the total star-formation rate will be under-estimated. Using the FIR-estimated star-formation rate of Paper I for a 1-100 M_{\odot} Salpeter IMF, $1920 \mathcal{M}^{-1} M_{\odot} \text{ yr}^{-1}$, and the measured half-light radius of the $H\alpha$ emission, we find $\Sigma_{FIR, H\alpha} = 28 M_{\odot} \text{ yr}^{-1} \text{ kpc}^{-2}$. Using the FWHM of the CO emission line region to estimate the diameter of the star-forming region ($1.6'' \times 0.5''$ and $2.5'' \times 0.5''$ Downes 2006), we find a similar star-formation intensity of $\Sigma_{FIR, CO} = 48 - 30 M_{\odot} \text{ yr}^{-1} \text{ kpc}^{-2}$. Both estimates are within the range of the $80 \pm 20 M_{\odot} \text{ yr}^{-1} \text{ kpc}^{-2}$ that Tacconi et al. (2006) found for a sample of SMGs using high resolution CO observations. (To mitigate against the considerable uncertainties in calibrating star-formation intensities from surface brightnesses, we note that the FIR luminosity of J1 from Paper I, $L_{FIR} = 2.3 \times 10^{13} \mathcal{M}^{-1} L_{\odot}$, and the CO radius of Downes (2006), correspond to a surface brightness of $S_{FIR} = 7.3 - 18 \times 10^{10} L_{\odot}$ in J1, compared to a 90% percentile of the effective surface brightness, $S_{e,90} = 2 \times 10^{11} L_{\odot} \text{ kpc}^{-2}$, given by Meurer et al. 1997).

In spite of the large uncertainties of each method, none of the estimates for J1 exceeds the star-formation intensities in low redshift “maximal burst” galaxies.

The most fundamental physical motivation to posit a stringent upper bound to the star-formation rate in a self-gravitating system comes from causality. This limit is given by consuming all of the gas (modulo a star-formation efficiency per unit gas mass) within one dynamical time, either a crossing or free fall time scale (see, e.g., Lehnert & Heckman 1996b). Tacconi et al. (2006) find that none of the SMGs, including SMMJ14011+0252, violate causality arguments. Specifically, within the context of such a hypothesis, Tacconi et al. find that SMGs form stars with efficiencies similar to those seen in local galaxies and star-forming regions, 0.1-0.3, and within a few dynamical timescales. Our results here suggest that SMMJ14011+0252 does not violate the stringent causality limits either.

5.2. *No “new mode” of star-formation*

At low redshift, only ULIRGs reach similarly large infrared luminosities as SMGs, $L \gtrsim 10^{12} L_{\odot}$, whose properties are typically attributed to the effects of massive gas collapse during major mergers (Sanders & Mirabel 1996). Motivated by the extended nature of star formation in SMMJ14011+0252, Goldader et al. (2002) hypothesize that there might be an intrinsically more efficient mechanism of star formation at high redshift, with

no equivalent in the local universe, which does not require a major merger to trigger extreme star formation.

Our data do not confirm this hypothesis, in fact, they rather point towards SMMJ14011+0252 being a merger (§4.2). As discussed previously, our data do not indicate a higher intensity of star formation than at low redshift, and the half-light radii of $H\alpha$ emission are similar to those of low-redshift ULIRGs, correcting for gravitational magnification of SMMJ14011+0252. For example, the largest $H\alpha$ half-light radius we find in the data set of Colina, Arribas, & Monreal-Ibero (2005), in the same way as for SMMJ14011+0252 (see above), is 2.1 kpc, compared to ~ 1.7 kpc for J1n (for a magnification $\mathcal{M} = 5$). We conclude that we do not find evidence for a peculiar, more efficient “high-redshift” star-formation mode in SMMJ14011+0252.

6. A STARBURST-DRIVEN SUPERWIND AT $Z = 2.6$

6.1. Properties of the Superwind

Actively star-forming galaxies with intensities exceeding $0.1 M_{\odot} \text{ yr}^{-1} \text{ kpc}^{-2}$ are known to drive “superwinds”, irrespective of redshift (Heckman 2003). SMMJ14011+0252 J1 easily surpasses this limit (§5) and can therefore be expected to drive such a wind. Blue asymmetries in emission line profiles, e.g. $H\alpha$ and $[\text{NII}]\lambda 6583$ line profiles are common in starburst galaxies in the local Universe with substantial evidence for driving vigorous outflows (Lehnert & Heckman 1996a), and are also the most common evidence for winds at high redshift. Velocity offsets of a few 100 km s^{-1} in UV absorption lines tracing the ISM relative to the systemic redshift are also frequently used as evidence for winds (Shapley et al. 2003; Swinbank et al. 2005). In J1, rest-frame UV absorption lines are blueshifted relative to $H\alpha$ by $\sim 500 \text{ km s}^{-1}$ (Ivison et al. 2000; Tecza et al. 2004), and we also observe blue wings of $H\alpha$ and $[\text{NII}]\lambda 6583$ emission lines in J1n (see the inset of Fig. 4). Gaussian fits to the residuals have relative offsets of $\sim -330 \text{ km s}^{-1}$ between line wing and core for the $H\alpha$ lines and $\sim -350 \text{ km s}^{-1}$ for $[\text{NII}]$ in J1n. About 10% of the $H\alpha$ flux is in the wing, and $\sim 25\%$ of $[\text{NII}]\lambda 6583$. J1s does not have a pronounced blue wing.

The wavelength-coverage and quality of our J1 data sets are outstanding for a strongly starforming galaxy at $z \sim 2.6$, allowing for a more detailed analysis to firmly establish that starbursts and outflows in high redshift galaxies are causally linked by the same basic mechanism as at low redshift. Starburst-driven winds at low redshift are caused by thermalized ejecta of supernovae and stellar winds producing an over-pressurized, expanding bubble of hot, X-ray emitting gas, which sweeps up, entrains, accelerates, and ionizes the ambient interstellar medium (Heckman et al. 1990). This results in high gas pressures and shock-like optical emission line ratios. Positive correlations between ionization state and line widths have been observed at low-redshift (e.g. Lehnert & Heckman 1996a; Rupke et al. 2005), implying that the relative importance of shock heating increases as the gas is accelerated to outflow velocities of a few hundred km s^{-1} , where the emission line luminosity rapidly increases with increasing shock speed (Dopita & Sutherland 1995).

For J1 we can investigate each of these properties explicitly. $[\text{NII}]\lambda 6583/H\alpha$ line ratios are ~ 0.7 in the integrated emission of J1n, which is generally higher than ob-

served in HII regions (photo-ionization by massive stars), and can be easily caused by shocks. The $[\text{NII}]/H\alpha$ line ratio in the wings of J1n is 0.83 indicating a higher shock contribution in the outflowing gas. We also find a good correlation between $[\text{NII}]\lambda 6583/H\alpha$ ratio and $[\text{NII}]\lambda 6583$ line width in J1n (left panel of Fig. 10), but not in J1s. We also find no correlation with $H\alpha$ line widths (right panel of Fig. 10), similar to nearby “superwind” galaxies (Lehnert & Heckman 1996a).

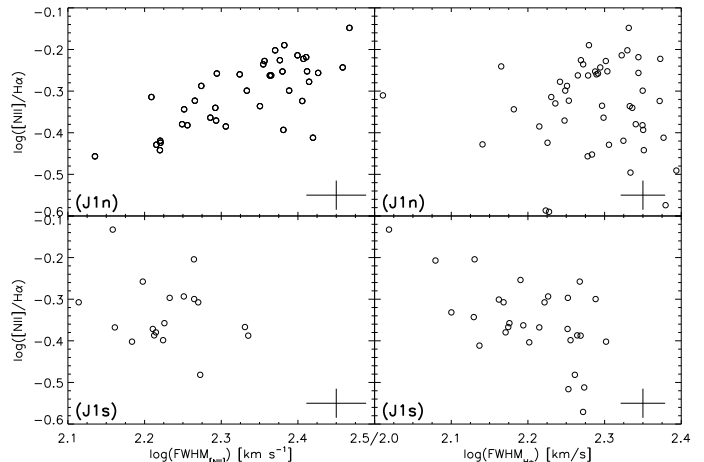


FIG. 10.— $[\text{NII}]\lambda 6583/H\alpha$ line ratio as a function of $[\text{NII}]$ and $H\alpha$ FWHM for J1n (top, right and left panels) and J1s (bottom, right and left panels). $[\text{NII}]$ FWHM and line ratio are correlated in J1n, but not in J1s. For the $H\alpha$ FWHM, no similar correlation is found in J1n or J1s. Interestingly, the correlation seen in the $[\text{NII}]\lambda 6583/H\alpha$ line ratio and $[\text{NII}]$ FWHM for J1n is virtually identical in the range of values and the correlation to that observed in a sample of local starburst galaxies exhibiting superwinds (Lehnert & Heckman 1996a, their Fig. 17). Crosses indicate typical uncertainties.

With the electron densities derived in §4.1.1 we estimate the pressure of the electron gas using the conversion given in Lehnert & Heckman (1996a) and considering that much of the $[\text{SII}]$ and $[\text{OII}]$ lines fluxes are produced in partially ionized zones of the nebulae (Shull & McKee 1979): $P \approx 4 \times 10^{-12} n_e \text{ dyn cm}^{-2}$, or $P \approx 2 \times 10^{-9} \text{ dyn cm}^{-2}$ for the electron densities $\sim 400 \text{ cm}^{-3}$ derived in 4.1.1. This is in excellent agreement with the pressures in the nuclei of nearby starburst galaxies with evidence for driving superwinds (Lehnert & Heckman 1996a), and is factors $\sim 10^{3-4}$ higher than the pressure of the local ISM in the Milky Way, providing the necessary prerequisite for an expanding or outflowing gas bubble.

However, compared to low-redshift starburst galaxies, the wind in J1 seems to have a relatively high surface brightness. Maximum $H\alpha$ surface brightnesses in the low redshift sample of Lehnert & Heckman (1996a) are $\lesssim 800 L_{\odot} \text{ pc}^{-2}$ and for our cosmology would correspond to an observed flux $f_{obs} = 2.3 \times 10^{-21} h_{70}^{-2} \text{ W m}^{-2} \text{ pix}^{-1}$ at the redshift of J1, about an order of magnitude lower than the total $H\alpha$ flux in the wing of J1 ($\sim 10\%$ of the total $H\alpha$ flux, or $\sim 1.1 \times 10^{-19} \text{ W m}^{-2} \text{ pix}^{-1}$). This might be due to a higher gas fraction in J1, leading to a larger covering factor of gas clouds that are being shocked. Tacconi et al. (2006) estimate a gas fraction of $f_{gas} \sim 0.4$ in SMGs supporting such speculation.

Since the wind causes a correlation between $[\text{NII}]\lambda 6583/H\alpha$ ratio and the $[\text{NII}]$ line width, we also investigate its impact on the overall velocity field

(Fig. 7), again using correlations between the spatially resolved emission line properties to localize and compare the signatures of mechanical heating and kinematic parameters. The upper and lower panels of Fig. 11 show the correlations between line properties for the $H\alpha$ and $[\text{NII}]\lambda 6583$ lines in J1n, respectively. The data are given separately for spatial pixels with high and low $[\text{NII}]/H\alpha$ ratios. Empty squares indicate spatial pixels where $[\text{NII}]/H\alpha < 0.55$, filled dots show spatial pixels where $[\text{NII}]/H\alpha > 0.55$. Line widths and fluxes are correlated for $[\text{NII}]$, tracing the stronger contribution of mechanical heating in the blueshifted $[\text{NII}]$ gas, but none of the other line properties appear to be correlated. In particular, the position of the line centroids are not correlated with flux or line width (middle and right panels), suggesting they are dominated by large-scale gravitationally-driven motion similar to low-redshift starburst galaxies (e.g., Lehnert & Heckman 1996a). This is the case for pixels with high and low $[\text{NII}]/H\alpha$ ratios. Fully consistent with the integrated spectrum (Paper I), this shows that gas ionization is dominated by the ionizing photons from the intense star-formation, and that the velocities traced by the $H\alpha$ line centroids are not overall significantly altered by the wind.

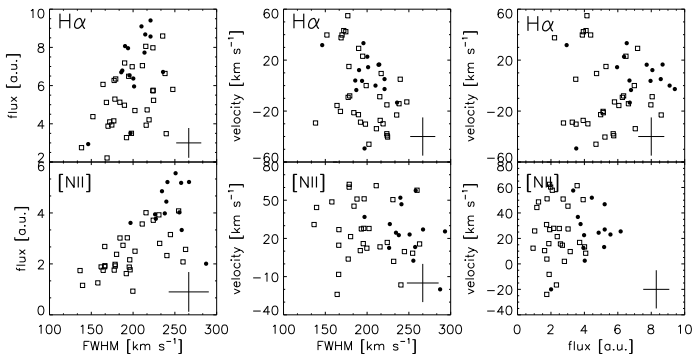


FIG. 11.— Emission line correlations for $H\alpha$ and $[\text{NII}]\lambda 6563$ in J1n. In the upper and lower panel of each column, we show the correlations for $H\alpha$ and $[\text{NII}]\lambda 6583$ respectively. Open squares in each diagram represent pixels with low ionization, $[\text{NII}]/H\alpha < 0.55$, whereas filled circles indicate pixels with $[\text{NII}]/H\alpha > 0.55$. Crosses indicate typical uncertainties.

6.2. Self Regulated Star-Formation?

As discussed previously, there are several arguments about what might be regulating star formation within galaxies (see also, e.g., Tacconi et al. 2006; Lehnert & Heckman 1996b), including negative feedback from the superwind, if the overpressurized bubble can plausibly provide pressure support. Can this hypothesis explain the variation of velocity dispersions in J1, and limit the rate of star-formation? Adopting a disk geometry, this scenario implies that gas collapse can be balanced if the momentum flux injection, \mathcal{P}_{wind} , is comparable to the midplane pressure, \mathcal{P}_{mid} . In hydrostatic equilibrium, \mathcal{P}_{mid} is,

$$\mathcal{P}_{mid} = \frac{1}{2} \pi G \Sigma_{tot} \Sigma_{gas} = 4.6 \times 10^{-10} \Sigma_{tot,9} \Sigma_{gas,8} \text{ dyn cm}^{-2}$$

where $\Sigma_{tot,9}$ and $\Sigma_{gas,8}$ are the surface mass densities of all of the matter and just the gas in units of

$10^9 M_{\odot} \text{ kpc}^{-2}$ and $10^8 M_{\odot} \text{ kpc}^{-2}$, respectively. We use the size of molecular emission ($\text{FWHM} = 2.2'' \times 0.5''$ Downes & Solomon 2003), the molecular gas mass estimated in Paper I (and references therein), and our dynamical mass estimate, $M_{dyn,J1} \sim 10^{11} M_{\odot}$ (see §8), to estimate a total midplane pressure, $\mathcal{P}_{mid} \approx 10 \times 10^{-9} \mathcal{M} \text{ dynes cm}^{-2}$. The pressure provided by the wind can be derived from the total momentum flux of the outflow. Following Heckman et al. (1990) and Lehnert & Heckman (1996a) we parametrize the momentum injection by the wind as $\dot{p}_{winds} \approx 3 \times 10^{34} \mathcal{L}_{\text{IR},11} \text{ dynes}$, where $\mathcal{L}_{\text{IR},11}$ is the infrared luminosity in units of $10^{11} L_{\odot}$. With the infrared luminosity estimated in Paper I, $2.6 \times 10^{13} \mathcal{M}^{-1} \mathcal{L}_{\odot}$, this implies a momentum flux injection rate of $8 \times 10^{36} \mathcal{M}^{-1} \text{ dynes}$, similar to the most powerful local starbursts (Heckman et al. 1990). With the above size estimate, we find $\mathcal{P}_{wind} \approx 15 \times 10^{-9} \text{ dynes cm}^{-2}$. This implies $\mathcal{P}_{wind} \approx 0.3 \mathcal{P}_{mid}$ and $\mathcal{P}_{wind} \approx 0.5 \mathcal{P}_{mid}$ for $\mathcal{M} = 5$ and 3, respectively. Although this is somewhat smaller than unity if taken at face value, given the large uncertainties this is clearly consistent with the notion that star formation may be self-regulated through its own feedback in the most powerful starbursts, in particular at high redshift.

7. THE BLUE COMPONENT J2 – INTRINSIC PROPERTIES AND A PROBE FOR THE DYNAMICAL MASS OF J1

Our data sets also include component J2 of SMMJ14011+0252, which is about $1.3''$ to the north-west from J1c. J2 is considerably bluer than J1 at observed optical wavelengths (e.g., Ivison et al. 2000). Smail et al. (2005) pointed out that its rest-frame UV colors are similar to those of $z \sim 3$ Lyman-break galaxies, although its redshift is relatively low for such a comparison. Our population synthesis fits (see §4.4) indicate a $\gtrsim 3 \times 10^8$ yr old stellar population with $4.5 \times 10^9 \mathcal{M}^{-1} M_{\odot}$ stellar mass and $A_V = 0.5$ mag. This implies an older and more massive stellar population than favored by Motohara et al. (2005), although it is nonetheless a consistent result, because Motohara et al. only compared their photometry with an instantaneous burst and a 10^9 yrs old continuous star-formation episode.

As noted by previous authors (e.g., Ivison et al. 2001; Tecza et al. 2004), the spectrum of J2 is blueshifted by $-160 \pm 18 \text{ km s}^{-1}$ with respect to J1. In addition to detecting $H\alpha$, we also identify $[\text{NII}]\lambda 6583$ line emission in the K band, and the $[\text{OIII}]\lambda\lambda 4959, 5007$ doublet in the H band. $H\beta$ was not detected in J2, probably because of a nearby strong night sky line (see Table 2 for the emission line properties).

These results differ from those of Motohara et al. (2005), who identified $H\beta$, but not $[\text{OIII}]$. The discrepancy is easily explained by the lower resolution of their data ($R = 210$) and unfortunate spectral positions of the emission lines ($H\beta$ is near a strong night-sky line, $[\text{OIII}]\lambda 5007$ lying within a set of a strong telluric absorption features). We measure a 3σ limit on the $H\beta$ flux, $F_{H\beta} \leq 9 \times 10^{-21} \text{ W m}^{-2}$, compatible with relatively low extinction as indicated by the blue, “LBG-like” colors of J2 (see e.g. Smail et al. 2005), $E(B - V) \sim 0.23$, and an extinction corrected (lensed) $H\alpha$ luminosity $L_{H\alpha} = 2.3 \times 10^{35} \text{ W}$, which corresponds to a star-formation rate of $\sim 18 \mathcal{M}^{-1} M_{\odot} \text{ yr}^{-1}$. For a magnification $\mathcal{M} \gtrsim 3$, the star-formation rate is $\lesssim 6 M_{\odot} \text{ yr}^{-1}$, lower than the

typical rates in UV-selected, star-forming BX galaxies at similar redshift (e.g. Erb et al. 2003), and two orders of magnitude less than the highest estimates of the star-formation rates in J1.

H α emission in J2 extends over $\sim 1.25'' \times 0.75''$ and is offset from the continuum peak by $\sim 0.4''$ to the northeast. Extracting both line and continuum information from the same data cube and the reasonable signal-to-noise of both the line and continuum emission imply that this offset is significant. We do not measure a significant velocity gradient in the H α line emitting gas, but measure an intrinsic FWHM = 66 ± 8 km s $^{-1}$, for a reasonable set of assumptions about the mass distribution, corresponds to a dynamical mass of $M_{dyn,J2} \sim 10^9 M_{\odot}$.

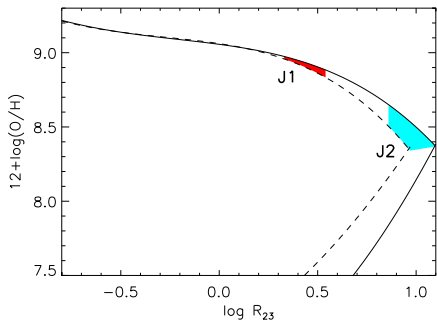


FIG. 12.— An estimate of the Oxygen abundances using the R_{23} method for J1 and J2. Solid and dashed lines indicate the calibration for high and low ionization, respectively. The red and aqua colored regions show the best estimate of $12+\log(\text{O}/\text{H})$ for J1 and J2 respectively and the ranges shown indicate the 1σ uncertainties in R_{23} . The values of $12+\log(\text{O}/\text{H})$ are double valued, but the relatively high $[\text{NII}]\lambda 6583/\text{H}\alpha$ ratio of both J1 and J2 suggest they lie on the upper branch. For J2, H β was not detected, and we used the 3σ upper limit on H β to determine the abundance in J2. Weaker H β moves R_{23} to even higher values and only marginally lower $12+\log(\text{O}/\text{H})$ due to J2 already lying near the upper envelope of R_{23} values.

We calculate the $[\text{O}/\text{H}]$ abundance of J2 from R_{23} to compare with the J1 abundance discussed in Paper I and to investigate whether the two components have similar or distinct evolutionary histories. As seen in Fig. 12, oxygen abundances are significantly different in J1 and J2, using the 3σ upper limit on H β to determine the abundance in J2. The $[\text{NII}]/\text{H}\alpha$ ratio of $\sim 0.23 \pm 0.07$ in J2 indicates that the upper branch is appropriate for estimating the metallicities.

The position of J2 in the emission line diagnostic diagrams of Osterbrock (1989) is also interesting. The $[\text{SII}]$ line doublet is not detected in J2. The upper limit on the H β flux only provides a lower limit for the $[\text{OIII}]/\text{H}\beta$ ratio. The emission line diagnostic ratios and excitation diagrams indicate comparably high ionization for J2, placing it near the limit of the AGN portion of the diagram. The distinct position of J2 indicates higher ionization or temperature compared to J1, and is likely a direct consequence of the lower metallicity of J2 (and perhaps a concomitant lower dust content).

The orbit of J2 can also be used to estimate an approximate dynamical mass of J1, which is particularly valuable, as the complex velocity field in J1 makes it difficult to robustly estimate a dynamical mass estimate

from the intrinsic kinematics. Following Paper I we add $6.5 \times 10^{10} M_{\odot}^{-1}$ in gas to the $\gtrsim 6 \times 10^{10} M_{\odot}^{-1}$ of stellar mass we found in §4.4. J1 appears to dominate the overall baryon budget by about an order of magnitude, which is consistent with the narrow line widths in J2 compared to J1n, and is certainly suggested by our astrometry which places the peak of the CO emission within the emission of J1n. Placing the barycenter on J1n, we use a simple virial estimate for the mass, $M_{J1}^{dyn} = \Delta V^2 R G^{-1} = 2. \times 10^{10} \Delta V_{100}^{J1J2} R_{kpc}^{J1J2} M_{\odot} \sim 1.0 \times 10^{11} M_{\odot}$, where G is the gravitational constant, $\Delta V_{100}^{J1,J2}$ is the relative velocity between J1 and J2 in units of 100 km s $^{-1}$, and R_{kpc}^{J1J2} is the distance between J1 and J2 in kpc. Since true inclination, eccentricity, form of the potential, etc., are all unconstrained and the physical separation is unknown, the true mass is likely factors of a few larger (both radius and velocity for example are seen in projection).

8. SURFACE MASS DENSITIES AND THE FUTURE EVOLUTION OF SMMJ14011+0252 AND OTHER SMGS

In addition to the high dynamical masses of SMGs (Genzel et al. 2003; Greve et al. 2005), mass densities (Tacconi et al. 2006), their luminosity-weighted ages, high star-formation rates, and possibly strong clustering indicate that they will likely evolve into massive early-type galaxies in cluster environments at low redshift (Smail et al. 2004, and references therein). Interestingly, the characteristics of local galaxies also seem highly dependent on their mass surface densities (and perhaps less so on their overall mass), as suggested by a recent analysis of Kauffmann et al. (2006). They studied nearly 400,000 low-redshift galaxies drawn from the Sloan Digital Sky Survey (SDSS), and find significant differences between the structural parameters of early and late type galaxies which does not strongly depend on the total mass of the galaxy. Namely, they find that concentration parameters $C > 2.5$ and stellar mass surface densities $\mu_{*} > 3 \times 10^8 M_{\odot} \text{ kpc}^{-2}$ correspond to the regime of galaxy spheroids and bulges, independent of the total stellar mass of these systems. Above this threshold of mass surface density, they find that star formation is increasingly suppressed (the specific star formation rate is low) and must have ceased many Gyrs ago. As a consequence, Kauffmann et al. (2006) hypothesize that with increasing compactness and surface density of the galaxy, stars were formed in short, vigorous episodes at high redshift, with extended periods of inactivity (Kauffmann et al. 2006, parameterize this in terms of a consumption time scale, $t_{cons} \propto \mu_{*}^{-1}$). Substantial growth at later epochs was then only possible through mergers of galaxies with low gas fractions. To identify SMM14011+0252 and other SMGs as “spheroids in formation”, it is therefore not sufficient to address their large masses or even their dynamical mass densities given their high gas fractions and unknown dark matter distributions. They must also have high stellar mass densities, short gas consumption time scales, and strong feedback suppressing further star-formation. Do SMGs have all these properties?

Our analysis of the stellar mass surface density in SMMJ14011+0252 J1 is that it is at the transition value of $3 \times 10^8 M_{\odot} \text{ kpc}^{-2}$ and the dynamical estimate of the

mass surface density in SMMJ14011+0252 J1 is $3 \times 10^9 M_{\odot} \text{ kpc}^{-2}$, well above the transition. The stellar masses ($\langle M_{\text{stellar}} \rangle = 3 \times 10^{10} M_{\odot}$) and average half-light radius ($\sim 5 \text{ kpc}$) of a large sample of SMGs (e.g., Smail et al. 2004), suggest average stellar mass surface density of $\mu_{\star}^{\text{SMG}} = 4 \times 10^8 M_{\odot} \text{ kpc}^{-2}$. Similar estimates can be made from dynamical mass estimates and sizes from CO interferometric observations ($\sim 10^9 M_{\odot} \text{ kpc}^{-2}$ for stars, gas, and possible contributions from dark matter; Tacconi et al. 2006; Greve et al. 2005). It appears that SMMJ14011+0252 and SMGs in general have sufficiently high mass surface densities to be above the critical point in the study of Kauffmann et al. (2006).

Population synthesis fits of the stellar population of SMM14011+0252 yield ages of up to a few 100 Myrs, similar to the ages of typical radio detected SMGs with spectroscopic redshifts (\sim few 100 Myrs; Smail et al. 2004). Based on the infrared luminosity and the gas mass, we estimate a gas consumption time scale of about 30-40 Myrs for SMM14011+0252. From a larger sample of SMGs with CO detections, Greve et al. (2005) set a limit on the gas consumption time scale of $\gtrsim 40$ Myrs, consistent with that for SMM14011+0252. Thus individual SMGs appear to be forming most of their stars in intense bursts of moderate duration (a few 100 Myr). In addition, their star-formation appears to be highly “bursty” independent of the duration of the star-formation. The duty cycles of SMGs have been estimated through a variety of methods to about ~ 0.1 (Chapman et al. 2005; Bouché et al. 2005; Genzel et al. 2003; Tecza et al. 2004; Blain et al. 2004). Again, SMGs seem to form their stars in intense bursts of modest durations with long periods of relative inactivity. To explain the fractions of local galaxies with strong 4000Å breaks, Kauffmann et al. (2006) infer gas consumption time scales of ≈ 100 Myrs, similar to estimates of SMGs.

As discussed in §6, SMM14011+0252 is driving a vigorous superwind. While the importance of starburst driven winds to galaxy evolution is generally agreed upon, they are not thought to be powerful enough or to accelerate material to the escape velocities of the most massive galaxies (Heckman et al. 2000). However, SMM14011+0252 is driving a wind, which at the very least will lower the overall star-formation efficiency of SMM14011+0252 (see discussion in §5.1 and §6.2). If this is indeed a general characteristic of SMGs, then the role of winds in their ultimate evolution could be substantial.

Hence, the “submillimeter bright phase” of galaxies is characterized by high surface mass densities, above the interesting dividing point of the characteristics of local galaxies as found by Kauffmann et al. (2006). Their star formation appears to be episodic (duty cycle of ≈ 0.1) and of relatively short duration (few 100 Myrs, e.g., Smail et al. 2004), and they have evidence for feedback which we have suggested may regulate the intensity of their star-formation. This adds further evidence that SMGs do indeed have all the characteristics necessary to become local massive early type galaxies.

9. SUMMARY

We presented an integral-field study of the rest-frame optical emission line gas in the $z \sim 2.6$ SMMJ14011+0252 J1/J2 complex, allowing unprece-

ented insight into the nature of a high-redshift starburst and its outflow. Identifying J1c as a $z \sim 0.25$ interloper through Sersic profile and SED fitting, we removed the seeing-matched J1c contamination from the images, and find that J1n and J1s appear as individual components in all wavebands, at a projected distance of a few kpc. The positions of these two components are in excellent agreement with the distribution of H α emission in our SPIFFI H α map and also with the H α velocity field, which is reminiscent of two nearby co-rotating disks which are marginally resolved spatially. Including J2, SMMJ14011+0252 thus appears as a triple system. From the J2 orbital motion, we estimate a dynamical mass of $M_{\text{dyn}, J1} \sim 1.0 \times 10^{11} M_{\odot}$ for the J1n/J1s complex.

The dust-enshrouded J1n is the most massive component, as indicated by its stellar mass, $\sim \text{few} \times 10^{10} M_{\odot}$ (compared to $\sim 1 - 2 \times 10^9 M_{\odot}$ for J1s and J2), and the bright CO line emission, which coincides with J1n within the astrometric uncertainties. The starburst in J1n is “maximal” with similar intensity ($\lesssim 50 M_{\odot} \text{ yr}^{-1} \text{ kpc}^{-2}$) comparable to the apparent limit at low redshift. The H α half-light radius is similar to the H α half-light radii in low-redshift ULIRGs. Overall, star formation in J1n is intense, but its properties do not greatly differ from low-redshift ULIRGs, highlighting the similarity between SMGs and ULIRGs at optical wavelengths, i.e., in the extended gas. Given these similarities and the complex large-scale kinematics, J1 does not appear to be a good candidate for an alternative, highly efficient “high-redshift mode” of star-formation, but appears governed by similar rules as low-redshift galaxies with intense star-formation, although it may be “scaled up” (Tacconi et al. 2006).

The intense starburst in J1 drives a superwind, as evident from blue emission line asymmetries, offsets between rest-frame UV interstellar absorption lines relative to H α , and enhanced [NII] $\lambda 6583$ /H α line ratios in J1n. The [NII]/H α ratios correlate with [NII] line width, indicating an increasing contribution of mechanical heating as the gas is accelerated in the wind, similar to low redshift starburst-driven winds. Measured densities (from the [OII] $\lambda\lambda 3726, 3729$, [SII] $\lambda\lambda 6717, 6731$ doublets) indicate pressures of $\sim 2 \times 10^{-9} \text{ dynes cm}^{-2}$, similar to pressures estimated in the expanding bubbles of over-pressurized hot gas in local starburst galaxies. These results are a direct indication that the basic physics of starburst-driven winds are rather similar at low and at high redshift, and supports the approach of studying local starburst galaxies to better understand the basic mechanisms of high-redshift galaxy formation. The strong wind may explain why H α equivalent width and reddening in SMMJ14011+0252 are positively correlated, which is likely a sign of patchy extinction.

The bluer component of the SMMJ14011+0252 system, J2, is very different from J1, with mass $\sim 10^9 M_{\odot}$ estimated from the narrow emission lines and SED fitting. Its gas-phase oxygen abundance, measured from R_{23} , $12 + [O/H] = 8.5$, about 0.4 dex lower than in J1 (Paper I). This signals that the two galaxies have had independent evolutionary histories, and that J2 is likely going to be accreted by the more massive J1n.

The “submillimeter bright phase” of galaxies, which SMM14011+0252 is now in, is characterized by high sur-

face mass densities, their star formation appears to be episodic and of relatively short durations, and they have evidence for feedback. These are just the characteristics needed to form early type spheroid dominated galaxies in the local Universe (Kauffmann et al. 2006). We find that only J1n has the necessary stellar mass surface density $\mu_{\star} > 3 \times 10^8 M_{\odot} \text{ kpc}^{-2}$, while the blue components appear less concentrated. With their current star-formation time scales, however, it appears unlikely that they are likely to substantially change the final characteristics of the most massive component J1n.

We would like to thank I. Smail and D. Downes for interesting discussions on the properties of submm galaxies

and SMMJ14011+0252 in particular and D. Downes for providing mm maps of SMMJ14011+252 from his previous work and some in advance of their publication. We also thank R. Ivison for providing the radio map of SMMJ14011+0252 and its surroundings which proved crucial in obtaining the accurate astrometry presented here. We further thank him, Ian Smail, and Scott Chapman for enlightening discussions about the properties and nature of submm-selected galaxies. AJB acknowledges support as a Jansky Fellow from the National Radio Astronomy Observatory, which is operated by Associated Universities, Inc. under cooperative agreement with the National Science Foundation.

REFERENCES

- Baldwin, J. A., Phillips, M. M., & Terlevich, R. 1981, *PASP*, 93, 5
 Barger, A. J., Cowie, L. L., Smail, I., Ivison, R. J., Blain, A. W., & Kneib, J.-P. 1999, *AJ*, 117, 2656
 Blain, A. W., Smail, I., Ivison, R. J., Kneib, J.-P., & Frayer, D. T. 2002, *Phys. Rep.*, 369, 111
 Blain, A. W., Chapman, S. C., Smail, I., & Ivison, R. 2004, *ApJ*, 611, 725
 Bouché, N., Lehnert, M. D., & Péroux, C. 2005, *MNRAS*, 364, 319
 Bremer, M. N., Jensen, J. B., Lehnert, M. D., Schreiber, N. M. F., & Douglas, L. 2004, *ApJ*, 615, L1
 Bruzual, G., & Charlot, S. 2003, *MNRAS*, 344, 1000
 Chapman, S. C., Smail, I., Windhorst, R., Muxlow, T., & Ivison, R. J. 2004, *ApJ*, 611, 732
 Chapman, S. C., Blain, A. W., Smail, I., & Ivison, R. J. 2005, *ApJ*, 622, 772
 Colina, L., Arribas, S., & Monreal-Ibero, A. 2005, *ApJ*, 621, 725
 Dopita, M. A., & Sutherland, R. S. 1995, *ApJ*, 455, 468
 Downes, D. & Solomon, P. M. 2003, *ApJ*, 582, 37
 Downes, D., private communication
 Eisenhauer, F., et al. 2003, *Proc. SPIE*, 4841, 1548
 Erb, D. K., Shapley, A. E., Steidel, C. C., Pettini, M., Adelberger, K. L., Hunt, M. P., Moorwood, A. F. M., & Cuby, J. 2003, *ApJ*, 591, 101
 Erb, D. K., Steidel, C. C., Shapley, A. E., Pettini, M., Reddy, N. A., & Adelberger, K. L. 2006, *ApJ*, 644, 813
 Fabian, A. C., et al. 2000, *MNRAS*, 315, L8
 Frayer, D. T., et al. 1999, *ApJ*, 514, L13
 Genzel, R., Baker, A. J., Tacconi, L. J., Lutz, D., Cox, P., Guillobeau, S., & Omont, A. 2003, *ApJ*, 584, 633
 Goldader, J. D., Meurer, G., Heckman, T. M., Seibert, M., Sanders, D. B., Calzetti, D., & Steidel, C. C. 2002, *ApJ*, 568, 651
 Greve, T. R., et al. 2005, *MNRAS*, 359, 1165
 Heckman, T. M., Armus, L., & Miley, G. K. 1990, *ApJS*, 74, 833
 Heckman, T. M., Lehnert, M. D., Strickland, D. K., & Armus, L. 2000, *ApJS*, 129, 493
 Heckman, T. M. 2003, *Revista Mexicana de Astronomia y Astrofisica Conference Series*, 17, 47
 Ivison, R. J., Smail, I., Barger, A. J., Kneib, J.-P., Blain, A. W., Owen, F. N., Kerr, T. H., & Cowie, L. L. 2000, *MNRAS*, 315, 209
 Ivison, R. J., Smail, I., Frayer, D. T., Kneib, J.-P., & Blain, A. W. 2001, *ApJ*, 561, L45
 Kauffmann, G., Heckman, T. M., De Lucia, G., Brinchmann, J., Charlot, S., Tremonti, C., White, S. D. M., & Brinkmann, J. 2006, *MNRAS*, 367, 1394
 Kennicutt, R. C. 1998, *ARA&A*, 36, 189
 Lehnert, M. D. & Heckman, T. M. 1996a, *ApJ*, 462, 651
 Lehnert, M. D. & Heckman, T. M. 1996b, *ApJ*, 472, 546
 Lehnert, M. D., Förster Schreiber, N. M., & Bremer, M. N. 2005, *ApJ*, 624, 80
 Leitherer, C., et al. 1999, *ApJS*, 123, 3
 Liu, C. T., & Kennicutt, R. C. 1995, *ApJS*, 100, 325
 Meurer, G. R., Heckman, T. M., Lehnert, M. D., Leitherer, C., & Lowenthal, J. 1997, *AJ*, 114, 54
 Mihos, J. C., & Hernquist, L. 1996, *ApJ*, 464, 641
 Motohara, K., et al. 2005, *AJ*, 129, 53
 Nesvadba, N. P. H., et al. 2006a, *ApJ*, accepted, astro-ph/0606530
 Nesvadba, N. P. H., et al. 2006b, *ApJ*, accepted, astro-ph/0606527
 Osterbrock, D. E. 1989, *Astrophysics of Gaseous Nebulae and Active Galactic Nuclei*, (University Science Books: Mill Valley, CA)
 Pettini, M., Shapley, A. E., Steidel, C. C., Cuby, J., Dickinson, M., Moorwood, A. F. M., Adelberger, K. L., & Giavalisco, M. 2001, *ApJ*, 554, 981
 Pettini, M., & Pagel, B. E. J. 2004, *MNRAS*, 348, L59
 Rudnick, G., et al. 2003, *ApJ*, 599, 847
 Rupke, D. S., Veilleux, S., & Sanders, D. B. 2005, *ApJS*, 160, 115
 Sanders, D. B., & Mirabel, I. F. 1996, *ARA&A*, 34, 749
 Shapley, A. E., Steidel, C. C., Pettini, M., & Adelberger, K. L. 2003, *ApJ*, 588, 65
 Shull, J. M., & McKee, C. F. 1979, 227, 131
 Smail, I., Ivison, R. J., Owen, F. N., Blain, A. W., & Kneib, J.-P. 2000, *ApJ*, 528, 612
 Smail, I., Ivison, R. J., Blain, A. W., & Kneib, J.-P. 2002, *MNRAS*, 331, 495
 Smail, I., Chapman, S. C., Blain, A. W., & Ivison, R. J. 2004, *ApJ*, 616, 71
 Smail, I., Smith, G. P., & Ivison, R. J. 2005, *ApJ*, 631, 121
 Swinbank, A. M., Smail, I., Chapman, S. C., Blain, A. W., Ivison, R. J., & Keel, W. C. 2004, *ApJ*, 617, 64
 Swinbank, A. M., et al. 2005, *MNRAS*, 359, 401
 Takata, T., Sekiguchi, K., Smail, I., Chapman, S. C., Geach, J. E., Swinbank, M. A., Blain, A., Ivison, R. J., *ApJ*, accepted, astro-ph/0607580
 Tacconi, L. J., et al. 2006, *ApJ*, 640, 228
 Tecza, M., et al. 2004, *ApJ*, 605, L109 (Paper I)
 van Dokkum, P. G., Kriek, M., Rodgers, B., Franx, M., & Puxley, P. 2005, *ApJ*, 622, L13

TABLE 2
EMISSION LINES IN J1

Region (1)	ID (2)	λ_{rest} (3)	z (4)	λ_{obs} (5)	$FWHM_{obs}$ (6)	$FWHM_{int}$ (7)	flux (8)
J1n	H α	6563	2.5651 ± 0.00052	2.3397 ± 0.00047	23 ± 1	259 ± 19	2.03 ± 0.12
J1n	[NII]	6583	2.5654 ± 0.00053	2.3471 ± 0.00048	26 ± 2	305 ± 32	1.05 ± 0.07
J1n	[NII]	6548	2.5658 ± 0.00058	2.3349 ± 0.00053	31 ± 6	377 ± 75	0.53 ± 0.04
J1n	[SII]	6717	2.5654 ± 0.00068	2.3949 ± 0.00063	26 ± 10	296 ± 113	0.26 ± 0.03
J1n	[SII]	6731	2.5663 ± 0.00093	2.4001 ± 0.00087	32 ± 18	373 ± 209	0.29 ± 0.03
J1n	[OIII]	5007	2.5652 ± 0.00064	1.7851 ± 0.00045	14 ± 6	188 ± 87	0.17 ± 0.02
J1n	H β	4861	2.5657 ± 0.00061	1.7333 ± 0.00041	11 ± 5	118 ± 58	0.13 ± 0.02
J1n	[OII]	3727	2.5656 ± 0.00085	1.3289 ± 0.00044	16 ± 8	349 ± 179	0.21 ± 0.03
J1s	H α	6563	2.5656 ± 0.00052	2.3401 ± 0.00048	22 ± 2	240 ± 25	1.09 ± 0.07
J1s	[NII]	6583	2.5658 ± 0.00056	2.3474 ± 0.00051	22 ± 4	238 ± 51	0.47 ± 0.04
J1s	[NII]	6548	2.5667 ± 0.0013	2.3354 ± 0.0012	66 ± 27	835 ± 348	0.43 ± 0.03
J1s	[SII]	6717	2.5726 ± 0.00085	2.3997 ± 0.00079	33 ± 15	388 ± 181	0.28 ± 0.02
J1s	[SII]	6731	2.5578 ± 0.00066	2.3944 ± 0.00062	14 ± 9	104 ± 68	0.14 ± 0.03
J1s	H β	4861	2.5658 ± 0.00060	1.7333 ± 0.00041	14 ± 5	194 ± 72	0.17 ± 0.02
J1s	[OIII]	5007	2.5655 ± 0.00069	1.7853 ± 0.00048	13 ± 7	178 ± 102	0.11 ± 0.02
J1s	[OII]	3727	2.5669 ± 0.00094	1.3294 ± 0.00049	23 ± 10	506 ± 216	0.23 ± 0.02
J2	[OIII]	5007	2.5636 ± 0.00057	1.7843 ± 0.00040	13 ± 3	< 50	0.28 ± 0.04
J2	[OII]	3727	2.5649 ± 0.0007	1.3286 ± 0.0003	16 ± 5	< 50	0.09 ± 0.007
J2	H β	4861	0	0	0	0	< 0.09
J2	H α	6563	2.5635 ± 0.00055	2.3387 ± 0.00050	14 ± 3	< 50	0.31 ± 0.04
J2	[NII]	6583	2.5628 ± 0.0013	2.3454 ± 0.0012	24 ± 29	< 50	0.07 ± 0.02

NOTE. — Column (1) – Regions as defined in Fig. 1–3. Column (2) – Line identification with wavelength given in Column (3). Column (3) – Rest-frame wavelengths in Å. Column (4) – Observed wavelengths in μm . Column (5) – Redshift of the line calculated using the wavelength in Column (3). Column (6) – Full-width at half-maximum measured in Å. Column (7) – Intrinsic FWHMs corrected for instrumental resolution in units of km s^{-1} . Column (8) – Line fluxes in units of $10^{-20} \text{ W m}^{-2}$.